BASELINE STUDIES OF THE CLAY MINERALS SOCIETY SOURCE CLAY MONTMORILLONITE STx-1b

Elena Castellini[1], Daniele Malferrari[1],*, Fabrizio Bernini[1], Maria Franca Brigatti[1], German Rafael Castro[2,3], Luca Medici[4], Adele Mucci[1], and Marco Borsari[1]

[1] Department of Chemical and Geological Sciences, University of Modena and Reggio Emilia, Via Campi 103, I-41125 Modena, Italy
[2] SpLine, Spanish CRG BM25 Beamline at the ESRF, 6 Jules Horowitz, F-38043 Grenoble, France
[3] Instituto de Ciencia de Materiales de Madrid (ICMM), CSIC, C. Sor Juan Inés de la Cruz 3, E-28049 Madrid, Spain
[4] Institute of Methodologies for Environmental Analysis, National Research Council of Italy, C. da S. Loja-Zona Industriale, I-85050, Tito Scalo (Potenza), Italy

Abstract—For more than forty years, The Clay Minerals Society has dispensed a set of source clays which have enabled a large number of researchers to work on similar materials. Many of these source clays remained unchanged over the years but, conversely, other clays have gone out of stock and thus were replaced. This was the fate of montmorillonite STx-1a, which was replaced by STx-1b. Although STx-1a and STx-1b share many basic chemical and mineralogical features, some minor differences exist that can affect behavior. A baseline characterization of the source clay STx-1b, which was the objective of this study, was, therefore, necessary to provide researchers a tool useful not only for new investigation but also to compare new results obtained on STx-1b with literature data on STx-1a. This characterization was gained using traditional and advanced methods that included: 1) chemical composition (major and trace elements); 2) cation exchange capacity determination; 3) thermal analyses coupled with evolved gas mass spectrometry; 4) quantitative mineralogical characterization using powder X-ray diffraction and Rietveld-RIR (Reference Intensity Ratio) refinement; 5) X-ray absorption spectroscopy at the Fe K-edge; 6) diffuse reflectance ultraviolet-visible and infrared spectroscopies; and 7) ^{29}Si, ^{27}Al, and ^{1}H magic-angle spinning nuclear magnetic resonance measurements. According to this multi-analytical approach, the chemical formula for STx-1b is $^{[4]}(Si_{7.753}Al_{0.247})$ $^{[6]}(Al_{3.281}Mg_{0.558}Fe_{0.136}Ti_{0.024}Mn_{0.002})$ $^{[12]}(Ca_{0.341}Na_{0.039}K_{0.061})O_{20}(OH)_4$.

Key Words—Bentonite, Montmorillonite, STx-1b, Smectite, Source Clay, 2:1 Clay Mineral.

INTRODUCTION

Since 1972, The Clay Minerals Society has distributed clay mineral samples, made available through the Source Clays Repository, to provide similar materials for study. The first baseline description of the Source Clays was reported in a Data Handbook by van Olphen and Fripiat (1979). With regard to montmorillonite, the Na-rich montmorillonite SWy-3 (Crook County, Wyoming, USA) and the Ca-rich montmorillonite STx-1b (Gonzales County, Texas, USA) are currently the only two montmorillonite-containing Source Clays that are available.

Interest in the investigation of montmorillonite properties (untreated, pillared, and/or variously functionalized) spans many fields in both fundamental and applied sciences. For this reason, the Ca-rich source clay montmorillonite STx-1a is better known and frequently cited as STx-1, and has been deeply studied from several points of view. For example, fundamental properties like internal surface-area (Mercier and Detellier, 1994),

swelling and delamination behavior (Assemi *et al.*, 2015), the adsorption and intercalation properties of inorganic compounds (Castellini *et al.*, 2013) and organic compounds (Bernini *et al.*, 2015), and the performance of modified (Bernini *et al.*, 2017) and activated (Moronta *et al.*, 2002) clay minerals in various entrapping and catalytic mechanisms were thoroughly addressed to increment basic knowledge and also because of the great industrial uses of montmorillonite.

Many of the Source Clays have remained unchanged (some clays have been resampled, *e.g.* STx-1, STx-1a, SWy-1, and SWy-2); however, new hardware, software, and analytical techniques have produced several updated reports and research (*e.g.*, Costanzo and Guggenheim, 2001; Madejová, 2003; Bishop and Murad, 2004; Takahashi *et al.*, 2008; Ortega-Castro *et al.*, 2009; Finck *et al.*, 2015) on most of the available Source Clays. On the other hand, some Source Clays became depleted and were, therefore, replaced with other Source Clays. This was the fate of the Source Clay STx-1a that was out of stock and was replaced with STx-1b. Although STx-1a and STx-1b share many basic chemical and mineralogical characteristics, some minor differences exist that can affect applications and exploitation potential. Careful characterization of this clay mineral cannot, therefore, be neglected.

* E-mail address of corresponding author:
daniele.malferrari@unimore.it

The purpose of the present study was to provide a baseline characterization of Source Clay STx-1b using traditional and advanced methods, and to compare such characteristics with data reported in the literature for Source Clay STx-1a. A further purpose was to calculate the chemical formula of STx-1b, with other phases and impurities excluded, using the data from this multi-analytical approach.

MATERIALS AND METHODS

Sample STx-1b was obtained from the Source Clays Repository of The Clay Minerals Society. All experimental characterizations reported in this paper, if not otherwise stated, were performed on the "as received" material. All chemical compounds used for sample preparation and measurements (see next section for details) were of analytical grade (purity > 99%) or certified analytical standards.

The thermogravimetric (TG) and differential thermal analysis (DTA) measurements were performed using a Seiko SSC 5200 thermal analyzer (Seiko Instrument Inc., Tokyo, Japan) equipped with an ESS GeneSys Quadstar 422 quadrupole mass spectrometer (ESS Ltd, Cheshire, UK) which allowed the analysis of gases evolved during thermal reactions. Gas sampling for the spectrometer used an inert, fused silica capillary system that was heated to prevent gases from condensing. Gas analyses were performed to determine the evolved chemical species with changes in temperature or time during TG and DTA measurements. Background subtraction was used to obtain the point zero conditions before starting evolved gas analysis. Experimental conditions were as follows: a heating rate of 20ºC/min, heating range of $25-1150$ºC, data measurements at every 0.5 s, α-alumina powder as DTA reference material, and a purge gas of ultrapure He at a flow rate of 100 μL/min. Mass analyses were performed in multiple ion detection mode by measuring the m/z ratios (*i.e.*, the dimensionless ratio between the mass number (m) and the charge (z) of an ion), 17 and 18 for H_2O, 28 and 44 for CO_2, and 48, 64, and 66 for SO_2. These m/z ratios were selected because more intense signals that do not overlap are produced in each spectrum. The SEM (secondary electron multiplier) and Faraday cup detectors were employed at 1100 V with a one-second integration time for each measured mass. Definitive signals were, however, collected using the SEM detector. To provide a better comparison of the STx-1b thermogravimetric data with the data reported for STx-1a (Guggenheim and Koster van Groos, 2001; Bernini *et al.*, 2015), an additional measurement was made in air at a heating rate of 10ºC/min.

The X-ray diffraction powder (XRPD) patterns were collected from randomly oriented grain mounts at room temperature and at 375ºC using a Philips X'Pert PRO diffractometer (PANalytical B.V., Almelo, The Netherlands) equipped with an X'Celerator detector and HTK16 Anton Paar *in situ* heating apparatus (Anton Paar Korea Ltd., Seoul, Republic of Korea). Experimental conditions were as follows: the incident beam was Cu Kα radiation at 40 kV and 40 mA, with a Ni filter, 0.02 rad Soller slits, a 20 mm anti-scatter mask, a 1/4º anti-scatter slit, and a 1/4º divergence slit. The diffracted beam conditions were as follows: X'Celerator X-ray detector with a position sensitive detector (PSD), a 5.0 mm anti-scatter mask, 0.02 rad Soller slits, and a 480 s integration time in a continuous scan with a PSD length of 2.12º2θ, which corresponds to a step size of 0.0170º2θ. Measurements were collected in the $3-100$º2θ range, and the NIST SRM 676a standard alumina powder with a corundum structure was used as the internal standard for quantitative mineralogical analyses performed using the Rietveld-RIR method, the General Structure Analysis System (GSAS) software package (Larson and Von Dreele, 1994), and the EXPGUI user graphical interface (Toby, 2001). The amount of alumina standard added was 20% (w/w). The starting structural models of montmorillonite, illite, cristobalite, tridymite, and quartz were taken from Viani *et al.* (2002), Gualtieri (2000), Peacor (1973), Kihara (1981), and Smith and Alexander (1963), respectively. In the data refinement, the background was modeled using function 1 within the GSAS software, a Chebyschev polynomial of the first kind; peak shapes were modeled using the Thompson–Cox–Hastings pseudo-Voigt function (function 2); and the March-Dollase function was chosen as the intensity correction factor for the preferred orientations.

The XRPD patterns at room temperature were used to determine the amounts of cristobalite, tridymite, and quartz. The structural model of montmorillonite was used to improve the quantitative mineralogical refinement. The XRPD patterns at 375ºC were used to obtain the amounts of dehydrated montmorillonite (Gattullo *et al.*, 2016). After heating at 375ºC, the change in weight of the NIST SRM 676a alumina standard was assumed to be negligible (Men *et al.*, 2003). The illite sample reported in Gualtieri (2000) was selected as the starting structural model for dehydrated montmorillonite after tests using micas and other illites proved insufficient. The amount of montmorillonite was calculated using the percent interlayer water measured using thermogravimetric analysis.

The cation exchange capacities (CECs) were determined using the NH_3-electrode method (Borden and Giese, 2001). The NH_4^+ concentrations in the supernatants were measured using an ORION 95-12 gas-sensing electrode (ORION Research Inc., Jacksonville, Florida, USA) after conversion to NH_3. Two mL of ISA (Ionic Strength Adjustor) was added per 100 mL of the suspensions and standards immediately before measurement. Calibration was performed using a single meter reading of two standards with a 10-fold difference in

concentration to bracket the expected sample range. These standards were obtained by properly diluting a 1000 mg/L certificated NH_4^+ standard solution. The method of Borden and Giese (2001) quantifies the NH_4^+ released (*i.e.*, exchanged) from a NH_4^+–treated clay when it interacts with a Na^+ solution. Ammonium was also measured using TGA and elemental analyses to calculate the total NH_4^+ that was adsorbed by NH_4^+–treated clays and, thus, provided an additional data point on STx-1b NH_4^+ saturation behavior.

The Fe *K*-edge X-ray absorption spectra (XAS) were collected at the European Synchrotron Radiation Facility (ESRF, Grenoble, France) on the Spanish Beam Line (SpLine, BM25 Branch A). The storage ring was run under uniform mode conditions with the current working range of 180–200 mA. A Si(111) double-crystal monochromator was used to provide an energy resolution of $\Delta E/E \cong 1.4 \times 10^{-4}$ eV. For all spectra, a metallic Fe reference foil provided an energy calibration and energy reproducibility was determined to be ±0.05 eV. Data were collected both in transmission and in fluorescence mode at room conditions on about 10 mg of powdered samples mounted between two sheets of adhesive Kapton® polyimide film. The spectra were recorded over a full energy range of about 800 eV across the Fe absorption *K*-edge with a 0.5 eV energy step in the X-ray Absorption Near-Edge Structure (XANES) region (7080–7160 eV) and 0.03 Å^{-1} in the Extended X-ray Absorption Fine Structure (EXAFS) region up to 15 Å^{-1} (7160–7900 eV). The XAS measurements were aimed to identify the presence of divalent and trivalent Fe and to check for tetrahedral (Fe(III)) or octahedral (Fe(II), Fe(III)) coordination (XANES region of the spectrum) and to identify the nature of the first neighboring atoms of Fe (EXAFS region). The reference compounds Fe_2O_3 (natural hematite), $Fe_2(SO_4)_3 \cdot nH_2O$, and $FeSO_4$ were measured to help interpret the STx-1b spectrum. Data reduction and analyses were performed using the Athena/Artemis interface of IFFEFIT software (Newville, 2001; Ravel and Newville, 2005). The XANES regions of the spectra were normalized in absorbance using a Victoreen function for atomic absorption based on the average absorption coefficient (Wilke *et al.*, 2001).

The diffuse reflectance (DR) UV-Vis-NIR measurements were performed using a V-570 Jasco Instruments spectrophotometer (Jasco Europe, Lecco, Italy), equipped with a Jasco model ISN-470 integrating sphere attachment in the λ =190 to 2000 nm range using $BaSO_4$ as a reference.

The FTIR measurements were performed using a Jasco Instrument FT/IR 4700 (resolution: 0.4 cm^{-1}) on dried STx-1b sample. The sample was maintained in a silica gel drier, dispersed in a KBr pressed disk (typically 2% w/w), and measured. To decrease the effect of the H_2O signal, an appropriate amount of clay was heated overnight at 180ºC and dispersed in KBr. The obtained disk was heated again at 180ºC overnight and used immediately for the FTIR measurement.

The NMR measurements were recorded at 300 K with an AVANCE III HD 600 Bruker spectrometer (Bruker, Rheinstetten, Germany) equipped with a 2.5 mm H/X CP-MAS probe operated at 600.13, 156.38, and 119.22 MHz for ^{1}H, ^{27}Al, and ^{29}Si, respectively. Samples were packed into a 2.5 mm zirconia rotor and spun at different magic-angle spinning (MAS) rates that depended on the experiment. The ^{29}Si NMR spectrum was obtained at 8 and 33 kHz MAS rates using single-pulse excitation with a 60 kHz spectral width, 40 s relaxation delays, 2 μs 35º pulse, 4k data points, and 1800–1300 scans. A cross polarization-MAS (CP-MAS) ^{29}Si NMR spectrum was obtained at a 8 kHz MAS rate using the standard Bruker CP sequence with 60 kHz spectral width, 4 s relaxation delay, 2.7 μs 90º ^{1}H pulse, rf field strength of about 62 kHz for Hartmann-Hahn match, 1 ms contact time, 4k data points, and 1k scans. The ^{27}Al NMR spectra were obtained at 15 or 30 kHz MAS rates using single-pulse excitation with a 188 kHz spectral width, 2 s relaxation delay, 0.5 μs 45º pulse, 4k data points, and 5k scans. Multi-quantum (MQ) MAS NMR spectra were recorded with a standard pulse sequence and a zero-quantum filter based on the excitation of the triple-quantum coherence. The excitation, conversion, and 90º selective pulses were 2.6, 0.8, and 19 μs, respectively. Other parameters were: 1 s relaxation delay, 20 μs zeta-filter delay, 188 kHz spectral width, 2 s relaxation delay, 4k data points, and 4k to 1k scans. The same parameters were used for the 2D experiments apart from 80 traces and a 30 kHz spectral width in the *f1* dimension. The ^{1}H{^{27}Al} cross polarization (CP) spectrum was acquired at 33 kHz MAS rate with a standard sequence for CP, exciting ^{27}Al and detecting ^{1}H magnetization developed after a 1 ms contact time. The ^{1}H NMR spectra were obtained at a 33 kHz MAS rate, using single-pulse excitation with a 200 kHz spectral width, 10 s relaxation delay, 2.7 μs 90º pulse, 4k data points, and 32 scans. The empty rotor ^{1}H spectrum was subtracted to compensate for baseline distortions and background effects. All chemical shifts were referenced by adjusting the spectrometer field to the value corresponding to 38.48 ppm chemical shift for the deshielded line of the adamantane ^{13}C NMR signal. With this setting, the TOPSPIN software (Bruker Biospin, Rheinstetten, Germany; Goldman *et al.*, 1992) generates data sets with the peak positions correctly calibrated according to IUPAC recommendations (Harris *et al.*, 2001) for all nuclei. The chemical shifts had an estimated accuracy of ±0.1 ppm. The MQMAS Analysis Module 1.0.2 of TOPSPIN 3.2 was used for the interpretation of MQMAS ^{27}Al NMR spectra. Deconvolution of ^{29}Si and ^{1}H NMR spectra was obtained with MNOVA 9.1.0 software (2012 Mestrelab Research S.L., Santiago de Compostela, Spain).

Chemical analyses of major elements and several minor elements were performed on pressed pellets of the clay mineral with a wavelength dispersive Philips PW

1480 X-ray fluorescence (XRF) spectrometer (Philips, Amelo, The Netherlands) using the methods of Franzini *et al.* (1975) and Leoni and Saitta (1976) to determine element concentrations. With this method, the fluorescence intensity I_j of element j in a sample containing N elements is related to the mass absorption coefficients of the sample by the formula:

$$I_j = \frac{C_j}{\sum_{i=1}^{N} K_{j,i} C_i}$$

where C_j and N are the concentrations of the elements and the number of elements in the sample, respectively, and $K_{j,i}$ are the absorption coefficients (Leoni and Saitta, 1976). Loss on ignition (LOI) was obtained from thermogravimetric measurements. The elemental analyses (C, N, S) were performed using a Model 1106 Carlo Erba Elemental Analyzer (Carlo Erba Instrument, Milano, Italy).

RESULTS AND DISCUSSION

Thermal analyses and evolved gas mass spectrometry

The thermogravimetric (TG) and the TG first derivative (DTG) curves of STx-1b measured in air using a heating rate of 10ºC/min (Figure 1) showed three thermal events with DTG curve maxima at 83, 154, and 699ºC. The first two reactions were attributed to the dehydration of the interlayer, whereas the reaction at 699ºC corresponded to the loss of octahedral sheet hydroxyl groups (Bish and Duffy, 1990). The two dehydration reactions were related to the thermal removal of outer sphere water molecules (10.57% weight loss maximum at 83ºC) and inner sphere water molecules (1.68% weight loss maximum at 154ºC). The

weight loss due to dehydroxylation (reaction maximum at 699ºC) was 2.64%; no other relevant thermogravimetric events were observed at temperatures greater than 700ºC, and cumulative weight loss at 1150ºC was 15.41%. This interpretation was also confirmed by evolved gas mass spectrometry (Figure SM-1, Supplemental Materials section (deposited with the Editor-in-Chief and available at https://www.clays.org/Journal/JournalDeposits.html)) which showed that the three reactions noted above only involved the release of water (m/z =18). The small shift in the temperature of the three maxima (Figure 1, Figure SM-1) was related to a more rapid heating rate (20 instead of 10ºC/min), which yielded better detection of evolved gases. To assure consistency in the data collected in air at 10ºC/min with data collected with a He flow at 20ºC/min, a He measurement at a heating rate of 10ºC/min was performed to compare with the measurement in air. This experiment generated curves that paralleled those obtained in air (Figure SM-2). A small thermal shift was observed for dehydration reactions with maxima at 71 and 142 and at 83 and 154ºC for samples heated in He and in air, respectively. This thermal shift was related to He, which promoted the formation of an anhydrous atmosphere, speeded up the removal of water, and, thus, confirmed that the temperature of a thermal event that involves water is influenced by the fugacity of water (Guggenheim and Koster van Groos, 1992). The DTA curve (Figure 1) suggested that the two observed high-temperature thermal events may be related to partial melting (peak at 885ºC) and recrystallization (inflection at about 1005ºC) as was previously reported for STx-1a by Guggenheim and Koster van Groos (2001) at approximately the same temperatures (894 and 1008ºC).
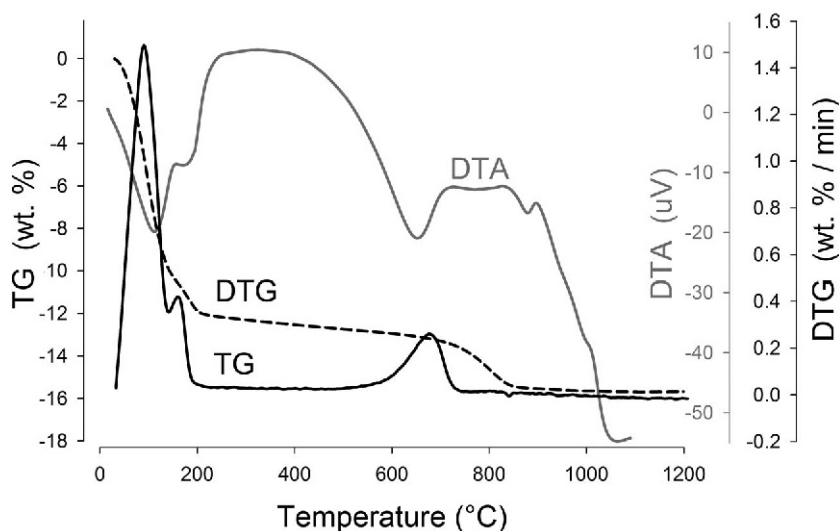

Figure 1. Differential thermal analysis (DTA, solid gray line), thermogravimetric analysis (TG, solid black line), and the TG first derivative (DTG, dashed black line) of STx-1b measured in air using a heating rate of 10ºC/min.

Quantitative X-ray powder diffraction

The quantitative mineralogical analysis of STx-1b (Table 1, Figure 2) revealed a large amount of montmorillonite (73%), important amounts of tridymite (11.6%) and cristobalite (12.8%), a very small amount of quartz (0.12%), and a small amount of an amorphous phase (2%). A small amount of quartz (3.0%) was also reported for STx-1a by Chipera and Bish (2001) who also measured a smaller amount of montmorillonite (67%) than in STx-1b. In addition, they found other phases, such as opal, feldspar, kaolinite, and probably talc, that were not found in STx-1b. Quantitative XRPD results agreed well with the thermal data, which showed no other thermal event than those due to montmorillonite thermal decomposition. No CO_2 (m/z = 44) and SO_2 (m/z = 64) release was observed (Figure SM-1), which indicated the absence of (or negligible amounts) amorphous carbonate and sulfate species. The small amount of quartz found using the Rietveld-RIR refinement explains the absence of a thermal event in the DTA curve at the transition temperature (573°C) of trigonal α to the high-temperature hexagonal β form of quartz.

Table 1. Quantitative mineralogical composition of STx-1b. The standard deviation σ_Q (in parenthesis) of the weight percent Q of each phase was calculated using the GSAS software quantitative refinement output file values. The formula $\sigma_Q = \{[(\sigma_a/a)^2 + (\sigma_b/b)^2]^{1/2}\} \, Q$ (Young, 1962) was used to calculate standard deviations, where a (phase weight fraction) and b (internal standard weight fraction) are the two variables that most affect Q values and σ_a and σ_b are the standard deviations of a and b. The montmorillonite standard deviation was obtained by matching illite-like phase contributions to the standard deviation (at 375°C) to the uncertainty due to interlayer water.

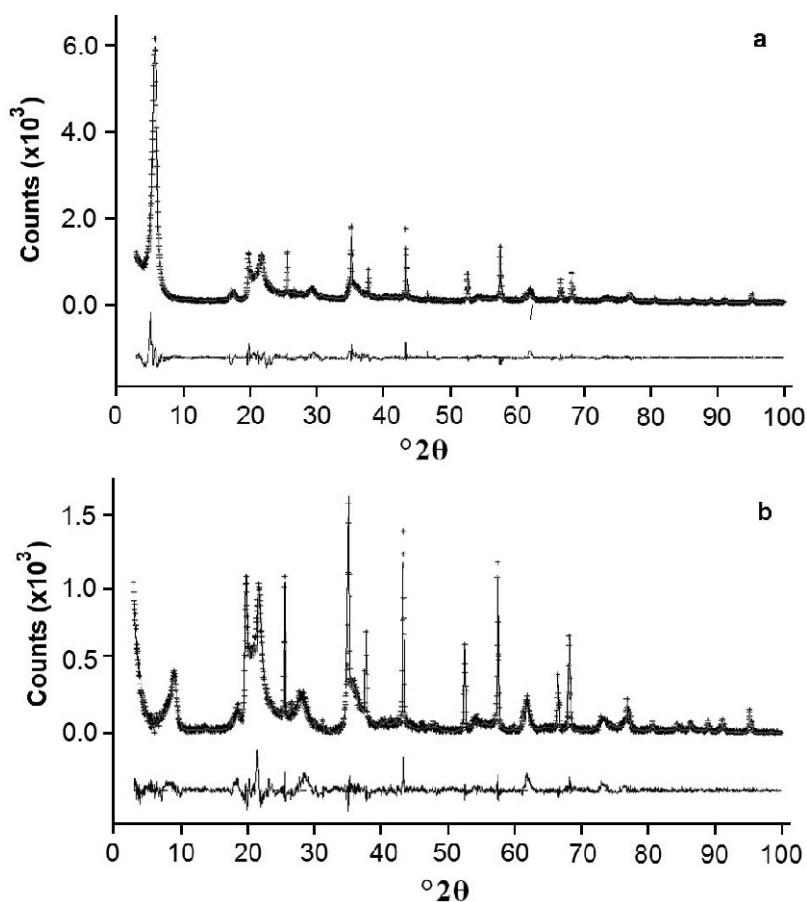|	Weight %
Montmorillonite	73 (1)
Cristobalite	12.8 (2)
Tridymite	11.6 (2)
Quartz	0.12 (4)
Amorphous	2 (1)
Sum	99.52

Figure 2. Observed XRPD (crosses), modeled XRPD (solid gray line), and XRPD difference pattern (bottom line) of refined STx-1b X-ray diffraction (XRPD) patterns with corundum NIST SRM 676a as internal standard measured at room temperature (a) and *in situ* at 375°C (b).

Cation exchange capacity

The NH_4^+-electrode method gave a CEC value of 66.1 (±2.1) meq/100 g for STx-1b using three replicates. This value was significantly lower than the CEC (89 meq/100 g) reported for STx-1a by Borden and Giese (2001). To confirm this result, another NH_4^+−exchanged STx-1b sample was prepared and tested for adsorbed NH_4^+ by thermogravimetric and elemental analyses. The TGA and DTG curves (Figure SM-3) of STx-1b showed a reaction between 197 and 402ºC that was not present in the natural sample (Figure 1). The 197−402ºC reaction was related to thermal desorption of NH_4^+. The corresponding weight loss (1.27%) indicated the loss of adsorbed NH_4^+ (74.7 mmol/100 g). The evidence nicely matched with N quantified by elemental analyses (1.06 ±0.04 w/w% from three replicates) that corresponded to 75.7 mmol/100 g of NH_4^+. The CEC values determined by thermal and elemental analyses were larger than the NH_4^+-electrode method values because thermal and elemental analyses measured all of the NH_4^+, whereas the method of Borden and Giese (2001) only detected the NH_4^+ replaced by Na^+.

XAS measurements

The STx-1b XANES spectrum (Figure 3) has three main features: i) a small pre-edge with maximum at 7113.5 eV, ii) a shoulder at 7124.7 eV, and iii) a crest with a maximum at 7133.7 eV.

The shapes and energy positions of these features are sensitive to the Fe redox state and coordination (Hahn *et al.*, 1982; Westre *et al.*, 1997; Finck *et al.*, 2015). The pre-edge is usually assigned to 1s→3d (quadrupolar) and/or to 1s→4p (dipolar) metal electronic transitions

(Westre *et al.*, 1997). The 1s→4p transition occurs only when Fe is in a non-centrosymmetric environment (Shulman *et al.*, 1976). A very weak pre-edge may also be observed in a centrosymmetric environment because it gains intensity from weak electric quadrupole coupling and/or from 3d−4p mixing (Hahn *et al.*, 1982). As reported by Wilke *et al.* (2001), the similarity between the XANES spectra of STx-1b and the Fe_2O_3 (natural hematite) and $Fe_2(SO_4)_3 \cdot nH_2O$ reference compounds (Figure 3) suggests that the Fe environment in STx-1b is similar to Fe(III) in octahedral coordination. The Fe *K*-edge measurements (Brigatti *et al.*, 2000; Manceau *et al.*, 2000; Vantelon *et al.*, 2003; Finck *et al.*, 2015) of several layer silicates with various Fe coordination and oxidation states showed that the spectra of samples with Fe(III) in octahedral coordination parallels the spectrum of STx-1b. In contrast, the STx-1b and $FeSO_4$ spectra in the XANES region (Figure 3) are dissimilar, which suggests the absence of divalent Fe. The EXAFS spectrum of STx-1b (Figure SM-4a) closely resembles the spectrum of STx-1a reported and critically described by Vantelon *et al.* (2003). The radial distribution function curve without correction for phase shifts (Figure SM-4b) had the most intense peak centered at 1.59 Å in agreement with Vantelon *et al.* (2003) and was assigned to the oxygen atoms that surround the octahedral Fe and indicated that oxygen atoms that define the octahedral coordination occupy the first neighbor positions. The other peaks in the 2−3.5 Å region originated from contributions of the nearest octahedral Fe, Al, and Mg and from the tetrahedral Si and Al located beside the octahedral sheet. The bands and peak in the 3.5−6 Å
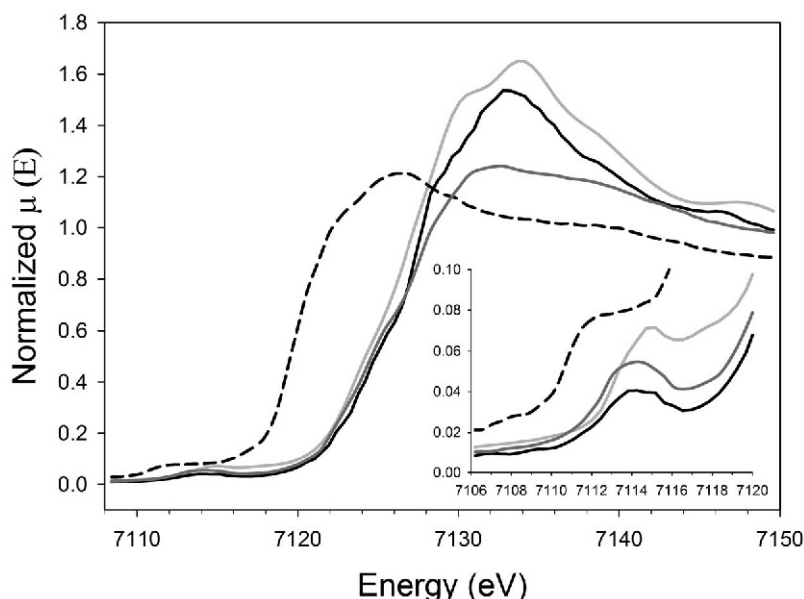

Figure 3. The XANES spectra of STx-1b (solid black line), natural hematite (solid light-gray line), $Fe_2(SO_4)_3 \cdot nH_2O$ (solid dark-gray line), and $FeSO_4$ (dashed black line) reference compounds with a magnified pre-edge region inset.

region predominantly resulted from two close tetrahedral and octahedral shells (Manceau *et al.*, 2000; Vantelon *et al.*, 2003).

DR UV-Vis-NIR spectroscopy

In the ultraviolet region of the STx-1b spectra (Figure 4), the very strong peak at 254 nm was attributed to the charge transfer transition oxo→Fe(III) with Fe(III) in an octahedral shell (Karickhoff and Bailey, 1973; Chen *et al.*, 1979), which is in agreement with the interpretation of the XANES spectra. Likewise, the absence of a peak at 212 nm suggested a lack of tetrahedral Fe(III). In contrast to some clays (Karickhoff and Bailey, 1973; Chen *et al.*, 1979), STx-1b also showed very weak absorption signals in the visible region (shoulders at 364, 485, and 646 nm, Figure 4). These absorption signals were related to the electronic transition that involves Fe(III). In particular, the shoulder at 364 nm is probably related to the $^6A_1 \rightarrow$ $^4E(^4D)$ ligand field transition of octahedral Fe(III) (Sherman and Waite, 1985). The signal at 485 nm was assigned to the transition $^6A_1 + {}^6A_1 \rightarrow {}^4T_1(^4G) + {}^4T_1(^4G)$ that involves the excitation of a Fe-Fe pair (this transition is observed in the 485−550 nm range for Fe(III) (oxyhydr)oxides), whereas the signal at 640 nm was assigned to the $^6A_1(^6S) \rightarrow {}^4T_2(^4G)$ ligand field transition of Fe(III) (Sherman and Waite, 1985).

The NIR region (Figure 4) has signals at 896 nm (11161 cm^{-1}, weak), 966 nm (10351.97 cm^{-1}, weak), 1156 nm (8666 cm^{-1}, weak), 1414 nm (7072 cm^{-1}), 1458 nm (6859 cm^{-1}, weak), 1795 (5593 cm^{-1}, weak), and 1910 nm (5236 cm^{-1}). The signal at 896 nm is similar to the one found for the Fe(III) (oxyhydr)oxides at about 900 nm (Sherman and Waite, 1985) and was assigned to the $^6A_1(^6S) \rightarrow {}^4T_1(^4G)$ ligand field transi-

tions of Fe(III). The weak band at 966 nm (10351 cm^{-1}) may, by analogy with studies on muscovite (Vedder, 1964) and kaolinite (Petit *et al.*, 1999), be related to the second overtone of the OH stretching fundamental modes of A1$_2$OH groups. The signals at 1156 nm (8666 cm^{-1}), 1414 nm (7072 cm^{-1}), 1458 nm (6859 cm^{-1}), and 1910 nm (5236 cm^{-1}) correspond to the signals of STx-1a at 8666, 7070, 6857, and 5247 cm^{-1} (Lu *et al.*, 2010). The signal at 8666 cm^{-1} was assigned to OH combination bands and may be related to the combination of $2\nu_1 + 2\delta OH$ or to OH stretching bands combined with H_2O vibrations. The signals at 7072 cm^{-1} and 6859 cm^{-1} are in the region of the first overtone of the hydroxyl fundamental ($2\nu_1$), but also the $2\nu_3$ and $\nu_1 + \nu_2$ bands can be observed in this frequency range. The signal at 5236 cm^{-1} was related to a water combination band (Lu *et al.*, 2010).

FTIR spectroscopy

The 3680−3550 cm^{-1} spectral range (Figure 5) has bands due to the stretching $\nu(OH)$ of octahedra with OH corners. As previously reported for STx-1a, the main band is shaped by two vibration effects at 3630 and 3624 cm^{-1} (Bernini *et al.*, 2017). The reason for this splitting is related to octahedral Mg for Al substitutions that originate in AlOHAl and AlOHMg domains that have different $\nu(OH)$ frequencies. The different local environments, especially the interactions with the surrounding oxygen atoms of the tetrahedral shell, play a role in affecting the frequency of these $\nu(OH)$ bands (Ortega-Castro *et al.*, 2009). The broad band at 3434 cm^{-1} was assigned to the $\nu(OH)$ modes of water molecules and originated from the overlapping of several $\nu(OH)$ bands produced by hydrogen bonds of different strength. The band at 1640 cm^{-1} is related to
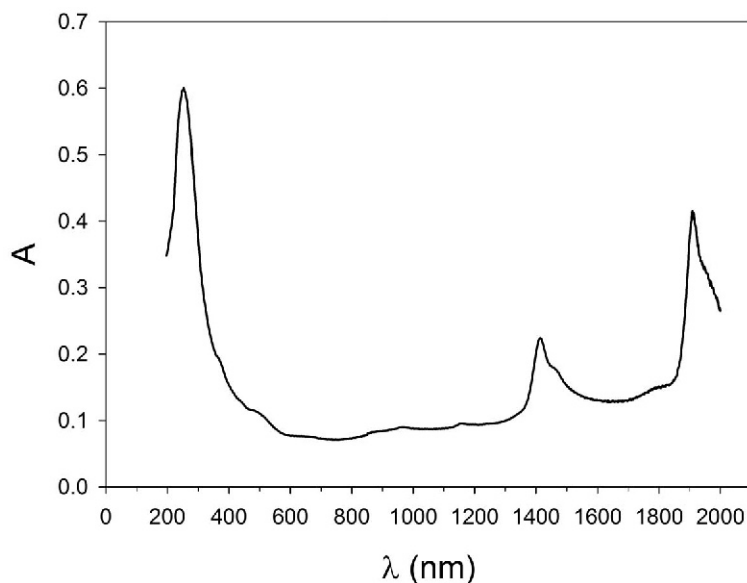

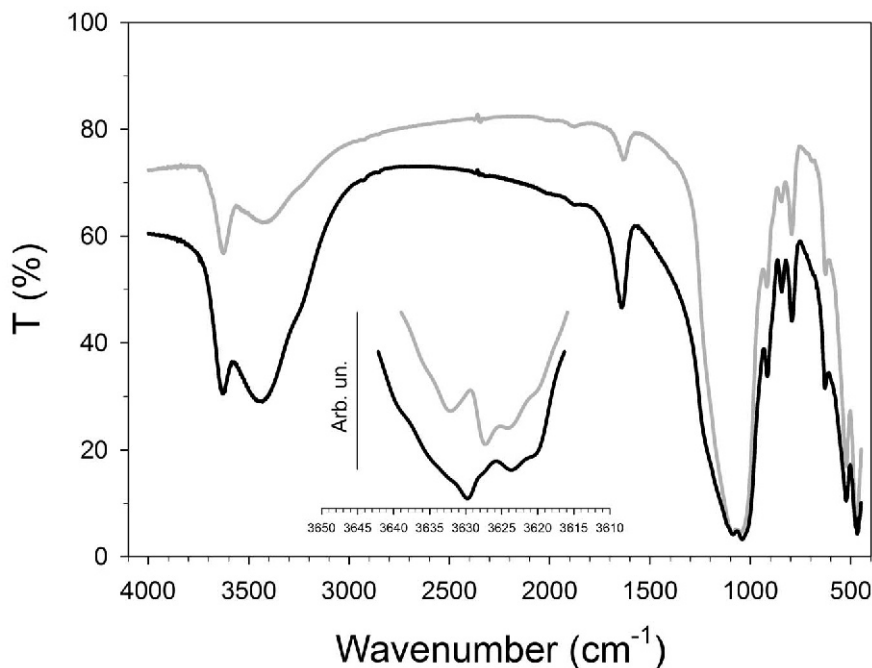Figure 4. The diffuse reflectance (DR) UV-Vis-NIR spectrum of STx-1b.

Figure 5. The FTIR spectra of STx-1b measured at room temperature (black line) and after heating at 180ºC (gray line) with a magnified $3650-3610$ cm^{-1} region as inset.

the bending of adsorbed H_2O (Che *et al.*, 2011) and the bands at 1086 and 1042 cm^{-1} are related to the stretching of Si(Al)−O bonds (Bishop *et al.*, 1994; Madejová *et al.*, 1998; Madejová, 2003; Bishop and Murad, 2004). The structural OH bending mode in montmorillonite is located between 700 and 950 cm^{-1} and depends on cation substitutions in the octahedral sheet. The STx-1b spectra showed: i) three well-defined signals at 916 cm^{-1} (AlOHAl bend), 844 cm^{-1} (AlOHMg bend and FeOHFe deformation), and 793 cm^{-1} (MgOHFe bend); and ii) a shoulder at 886 cm^{-1} related to the AlOHFe bend (Madejová *et al.*, 1998; Bishop *et al.*, 2002). The differences in the size of tetrahedral sites strongly affects silicate absorption features (stretching at 1086 and 1042 cm^{-1} and bending at 523 and 467 cm^{-1}) that occur as double bands (Bishop and Murad, 2004). The signal at 628 cm^{-1}, assigned to the Si-O-Si stretching of cristobalite (Finnie *et al.*, 1994; Madejova and Komadel, 2001), was also in agreement with XRPD measurements that revealed a large amount of this phase. These bands resemble those found for STx-1a (Bernini *et al.*, 2017). Unlike STx-1a, no band at 3692 cm^{-1} was observed even in the sample heated at 180ºC (Madejova and Komadel, 2001) and, thus, the presence of kaolinite in STx-1b can be excluded.

NMR measurements

The STx-1b sample was characterized using multinuclear (^{29}Si, ^{27}Al, and ^{1}H) NMR spectroscopy. The NMR Magic Angle Spin measurements performed here

are very innovative if not unprecedented in clay research fields and increase the range of the techniques employed for clay characterization.

The pulse-and-acquire ^{29}Si NMR spectrum (Figure 6) displayed two signals, a narrower signal at −93.3 ppm and a broader signal at −111.4 ppm. Under crosspolarization conditions, only the −93.3 ppm peak was detected, which confirms the assignment of this resonance to Si atoms in Q^3-type sites. The shielded signal (−111 ppm) was attributed to Q^4 type sites, is in agreement with XRPD data, and is related to tridymite and cristobalite, the signals of which were reported at −109/−111/−114 and −108.5/−111 ppm, respectively (De Jong *et al.*, 1987). The shielded component is nearly twice as broad as the deshielded component (370 *vs.* 760 Hz at half-height) because of the overlap of the Q^4 components of tridymite and cristobalite and to the number of Q^4 sites. The ^{29}Si NMR spectral shape is also compatible with two minor signals at around −88 and −102 ppm that account for 2−4% and 1−3% of the total area.

The ^{27}Al pulse-and-acquire and MQMAS 1D spectra (Figure 7a) displayed a major signal at 4.5 ppm that was assigned to octahedral Al and two minor resonances that were assigned to tetrahedral Al at 70.3 and 57.4 ppm. The signal at 70.3 ppm may be related to the Al in Q^3(3Si) sites, whereas the signal at 56 ppm is related to Al in Q^4(4Si) units in the structural framework of montmorillonite (Takahashi *et al.*, 2007). Signals at 70.3 and 57.4 ppm accounted for about 8% of the total area and this amount closely matched the tetrahedral Al
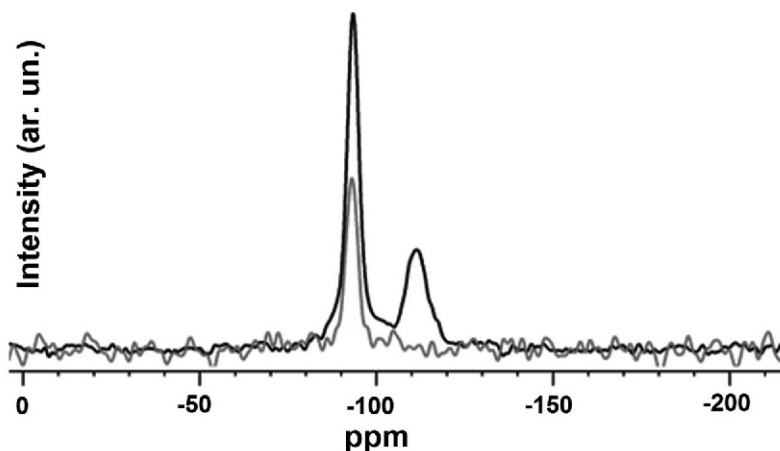
Figure 6. The ^{29}Si MAS NMR spectrum of STx-1b (black line) at 33 kHz MAS rate and the CP-MAS NMR spectrum acquired using a 1-ms contact time (gray line) at 8 kHz MAS rate.

determined from the difference between total and octahedral Al. The line width at half height of the major octahedral Al signal at 4.5 ppm is 1400 Hz, which is in agreement with that reported for other montmorillonites with Mg (Woessner, 1989). A 2D MQMAS spectrum (Figure 7b) was acquired to obtain more data on Al sites. Interpretation of Figure 7b indicated four octahedral Al sites with a variable quadrupolar-induced shift (Figure SM-5, Table 2). Three signals have similar isotropic chemical shifts (δ_{iso}), but differ in the second-

order, quadrupolar-effect parameter (P_Q) and in the induced quadrupolar shift (δ_{IQS}) (Amoureux *et al.*, 2002) The P_Q frequency increased from 2.9 to 5.7 MHz and δ_{IQS} shifted from 2.0 to 7.9 ppm (Table 2). The values of δ_{iso} and P_Q observed for STx-1b are higher than those reported for the Kunipia montmorillonite, which is believed to be *cis*-vacant (Takahashi *et al.*, 2008). The NMR data and dehydroxylation temperature (Figure 1) suggest that STx-1b has a *trans*-vacant structure. For all *trans*-vacant OH structures with only octahedral Al, one octahedral Al site should be observed in the MQMAS spectra. Here, the multiplicity of experimentally derived octahedral Al sites were greater than one and are believed to be due to the influence of cation distribution in the second neighbor as in *cis*-vacant structures (Takahashi *et al.*, 2008). The substitution of Al by Mg in octahedral sites increased the P_Q value of the remaining Al ions as a consequence of the distortion of the Al electric environment. This is due to a change of the electrostatic field gradient produced by the different ionic charge and to octahedron distortions by the different ionic radius of Mg (Woessner, 1989). Tetrahedral Al signals in the MQMAS spectra were too
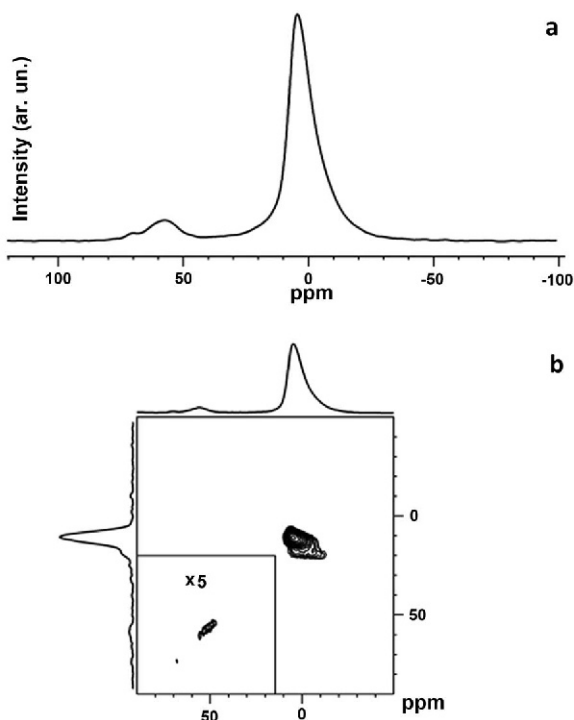

Figure 7. (a) ^{27}Al MAS NMR and (b) 2D MQMAS ^{27}Al spectra of STx-1b at 30 kHz MAS rate.

Table 2. Isotropic chemical shifts (δ_{iso}), quadrupolar products (P_Q), and induced quadrupolar shifts (δ_{IQS}) were determined from MQMAS experiments for the octahedral Al sites in STx-1b. These are the mean values of the fitting parameters obtained in four simulations based on a four-site model with both at >99.8% overlap.

	Site 1	Site 2	Site 3	Site 4
Integral%	12	31	24	33
δ_{iso} (ppm)	7.9	7.8	8.2	10.0
P_Q (MHz)	2.9	4.3	5.7	7.8
δ_{IQS} (ppm)	2.0	4.1	7.9	14.8

Table 3. Isotropic chemical shifts (δ_{iso}), quadrupolar products (P_Q), and induced quadrupolar shifts (δ_{IQS}) employed for MQMAS manual simulation of tetrahedral Al site signals in STx-1b reported in Figure 8.

	Site 1	Site 2	Site 3	Site 4	Site 5	Site 6
Integral%	26	10	17	7	23	17
δ_{iso} (ppm)	73.5	65.7	61.8	59.4	58.4	56.0
P_Q (MHz)	3.1	3.1	2.9	2.4	3.0	3.0
δ_{QIS} (ppm)	2.3	2.4	2.1	1.4	2.2	2.3

weak to be confidently fitted and, thus, only a rough visual estimate of the probable δ_{iso} and P_Q values was considered (Figure SM-5, Table 3). A fair determination of the spectral features was obtained using a P_Q value of about 3 MHz with η_Q in the range of $0-0.3$ and similar δ_{IQS} values for all tetrahedral sites. The ^{1}H NMR spectrum (Figure 8) completed the NMR spectroscopic study of STx-1b. A minimum of three components was required to closely reproduce the experimental line shape (Figure 8a). To confirm the assignment of proton

signals, the ^{1}H{^{27}Al}CP-MAS spectrum was acquired (Figure 8b). In this experiment, the magnetization produced by the initial excitation of the heteronucleus (^{27}Al) is transferred to the nearby ^{1}H nuclei *via* dipolar couplings during the CP contact time (1 ms). The CP-MAS spectra allowed protons close to Al (1.7 and 3.0 ppm) to be identified. These results agree with those reported by Cadars *et al.* (2012). Hence, the two shielded proton signals at 1.7 and 3.0 ppm were assigned to octahedral intra-sheet hydroxyl groups. The highest peak

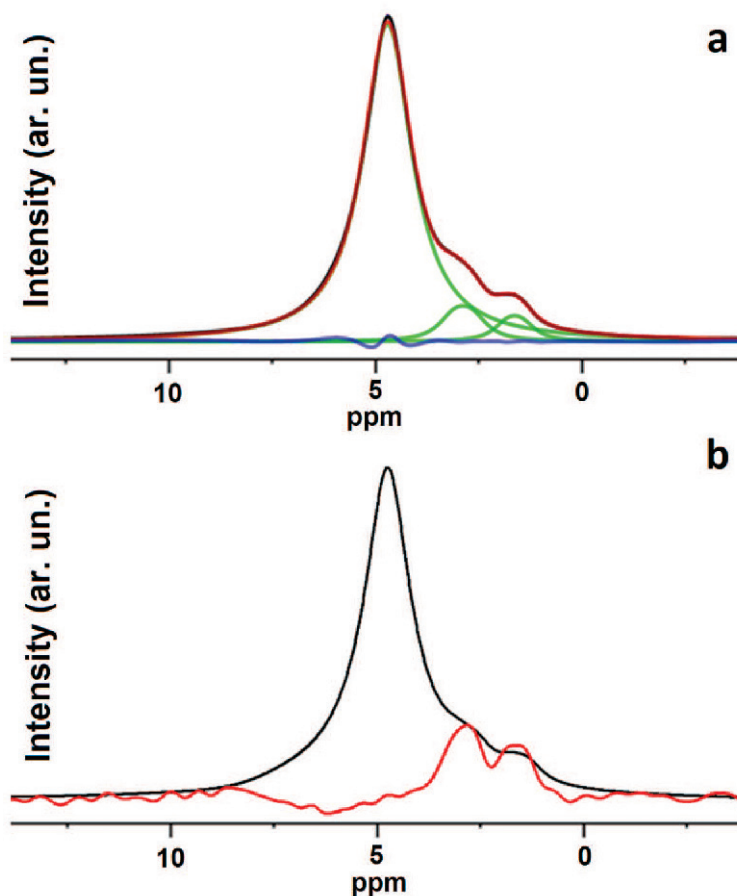Figure 8. (a) ^{1}H MAS NMR spectrum (black line) of STx-1b acquired at 33 kHz MAS rate, the spectral deconvolution of the three NMR spectral components (green lines), the sum of the deconvoluted NMR components (red line), and the residue (blue line). (b) ^{1}H MAS NMR spectrum (black line) and the ^{1}H{^{27}Al} CP-MAS NMR spectrum showing the octahedral hydroxyl resonances (red line) of STx-1b.

Table 4. Whole-rock chemical analyses (wt.%) of STx-1b major elements. The sample STx-1a measurements (Mermut and Cano, 2001) are reported for comparison. L.O.I. = Loss On Ignition.

	SiO_2	Al_2O_3	K_2O	Na_2O	MgO	CaO	Fe_2O_3	MnO	P_2O_5	TiO_2	L.O.I
STx-1b	64.76	14.95	0.24	0.10	1.87	1.59	0.90	0.01	0.01	0.16	15.41(*)
STx-1a	70.03	17.86	0.07	0.31	3.79	1.73	1.20	n.r.	0.01	0.26	4.63 (**)

(*) L.O.I. = thermogravimetric measurement of weight loss at 1150ºC (see Figure 1). (**) L.O.I. = weight loss between 100 and 1000ºC.

at 4.8 ppm (about 90% of the total area) was assigned to interlayer H_2O, the H_2O in the inner hydration shell of interlayer cations, and the SiOH protons. The proton chemical shifts observed for Ca-rich montmorillonite STx-1b are all deshielded in comparison to the Na-exchanged montmorillonite (Cadars *et al.* 2012) due to the different composition and, in particular, to the presence of interlayer Ca^{2+}.

Chemical analyses

The analytical chemical data (overall averages) for major elements (Table 4) are consistent with the other experimental results. In agreement with XRPD and NMR data, the large amount of Si is also ascribable to the tridymite and cristobalite in STx-1b (Table 1). The low amount of P (P_2O_5 = 0.01 wt.%) in STx-1b was due to impurities that were not identified using XRPD and was also reported for STx-1a (Mermut and Cano, 2001). Conversely, in agreement with XAS, DR UV-Vis-NIR, and FTIR spectroscopy, the Fe determined by XRF was assumed to be trivalent. Once again in agreement with XRPD data, the Ca, Na, and K may only be associated with montmorillonite and occupy interlayer positions. The sum of Ca, Na, and K was 65.0 meq/100 g, which is a value that is in nice agreement with the measured CEC (66.1 (±2.1) meq/100 g). The C, N, and S were below the detection limit of the instrument (150 ppm), which suggests negligible amounts of carbonates, sulfates, and nitrogen-bearing compounds in STx-1b. Montmorillonite (bentonite) is commonly used to test for heavy metal adsorption (*e.g.*, Brigatti *et al.*, 2004; Malferrari *et al.*,

2006, 2007, 2008; Zhu *et al.*, 2016). The analyses of trace elements that are most frequently cited as an environmental concern and hazard (*i.e.*, Ni, Co, Cr, V, Zn, Cu, Pb, As, Sb, Cd, Sn, and Hg) were, therefore, performed (Table 5) as well as elements of interest in petrographic investigations (Table 5).

CONCLUSIONS

The purpose of this paper was to provide a reference for any pure and applied clay science-related research involving the Source Clay STx-1b. The chemical formula of the main clay mineral component is useful in comparison with different clay minerals and can be an important achievement because many analytical techniques can provide quantitative data only if the formula of the investigated mineral is known. To obtain this goal, some constraints must be assumed. These include: i) Fe is trivalent and in octahedral coordination; ii) Mg, Mn, and Ti are in octahedral coordination; iii) P, S, and trace elements are not part of the montmorillonite; iv) Ca, Na, and K are only associated with montmorillonite and occupy interlayer positions; v) the tetrahedral and octahedral positions are 8 and 4, respectively; vi) except for dioctahedral vacancies, no vacant sites exist and, thus, the sum of cations is 12; vii) octahedral Al can be calculated as the difference between all octahedral positions and the sum of Mg, Fe, Ti, and Mn atoms; viii) the tetrahedral Al is the difference between the total and octahedral Al; and ix) the excess Si is attributed to SiO_2 polymorphs and to amorphous phases. From the

Table 5. Whole-rock chemical analyses (ppm) for selected trace elements in STx-1b. The available trace element measurements for sample STx-1a (Kogel and Lewis, 2001) are reported for comparison.

	Ni	Co	Cr	V	Zn	Cu	Pb	As	Sb	Cd	Hg
STx-1b	<10	3	<10	9	28	<50	10	7	<20	<50	<10
STx-1a	5.02	1.33	na	na	na	7.53	na	na	0.77	na	na

	Nd	La	Ce	Y	Rb	Cs	Zr	Sr	Ba	Sn	Cl
STx-1b	39	47	108	31	<40	<20	196	144	127	<20	<50
STx-1a	47.39	54.77	96.86	34.71	3.77	na	na	81.73	na	4.18	na

na = not available.

experimental data and given the assumed constraints, the calculated STx-1b montmorillonite chemical formula is: $^{[4]}(Si_{7.753}Al_{0.247})$ $^{[6]}(Al_{3.281}Mg_{0.558}Fe_{0.136}Ti_{0.024}Mn_{0.002})$ $^{[12]}(Ca_{0.341}Na_{0.039}K_{0.061})O_{20}(OH)_4$.

The findings of this work provide a background characterization that can be useful for researchers not only for new investigations, but also when they need to compare data obtained using STx-1b with literature data based on STx-1a. In particular, this data can be useful when the aim of research work goes beyond characterization and focuses on exploitation.

ACKNOWLEDGMENTS

REFERENCES

Amoureux, J.-P., Huguenard, C., Engelke, F., and Taulelle, F. (2002) Unified representation of MQMAS and STMAS NMR of half-integer quadrupolar nuclei. *Chemical Physics Letters*, **356**, 497−504.

Assemi, S., Sharma, S., Tadjiki, S., Prisbrey, K., Ranville, J., and Miller, J.D. (2015) Effect of surface charge and elemental composition on the swelling and delamination of montmorillonite nanoclays using sedimentation field-flow fractionation and mass spectroscopy. *Clays and Clay Minerals*, **63**, 457−468.

Bernini, F., Castellini, E., Malferrari, D., Borsari, M., and Brigatti, M.F. (2015) Stepwise structuring of the adsorbed layer modulates the physico-chemical properties of hybrid materials from phyllosilicates interacting with the μ-oxo Fe^{3+}−phenanthroline complex. *Microporous and Mesoporous Materials*, **211**, 19−29.

Bernini, F., Castellini, E., Malferrari, D., Castro, G.R., Sainz-Díaz, C.I., Brigatti, M.F., and Borsari, M. (2017) Effective and selective trapping of volatile organic sulfur derivatives by montmorillonite intercalated with a μ-oxo Fe(III)−phenanthroline complex. *Applied Materials Interfaces*, **9**, 1045−1056.

Bish, L.D. and Duffy, C.J. (1990) Thermogravimetric Analysis of Minerals. Pp. 96−157 in: *Thermal Analysis in Clay Science* (J.W. Stucki, D.L. Bish, and F.A. Mumpton, editors). Workshop Lectures, Volume 3, The Clay Minerals Society, Boulder, Colorado, USA.

Bishop, J.L. and Murad, E. (2004) Characterization of minerals and biogeochemical markers on Mars: A Raman and IR spectroscopic study of montmorillonite. *Journal of Raman Spectroscopy*, **35**, 480−486

Bishop, J.L., Madejová, J., Komadel, P., and Fröschl, H. (2002) The influence of structural Fe, Al and Mg on the infrared OH bands in spectra of dioctahedral smectites. *Clay Minerals*, **37**, 607−616.

Bishop, J.L., Pieters, C.M., and Edwards, J.O. (1994) Infrared spectroscopic analyses on the nature of water in montmorillonite clay. *Clay Minerals*, **42**, 702−716.

Borden, D. and Giese, R.F. (2001) Baseline studies of The Clay Minerals Society Source Clays: Cation exchange capacity measurements by the ammonia-electrode method. *Clays and Clay Minerals*, **49**, 444−445.

Brigatti, M.F., Colonna, S., Malferrari, D., and Medici, L. (2004) Characterization of Cu − complexes in smectite with different layer charge location: Chemical, thermal and EXAFS studies. *Geochimica et Cosmochimica Acta*, **68**, 781−788.

Brigatti, M.F., Lugli, C., Cibin, G., Marcelli. A., Giuli, G., Paris, E., Mottana, A., and Wu, Z. (2000) Reduction and sorption of chromium by Fe(II)-bearing phyllosilicates: Chemical treatments and X-ray absorption spectroscopy (XAS) studies. *Clays and Clay Minerals*, **48**, 272−281.

Cadars, S., Guegan, R., Garaga, M.N., Bourrat, X., Le Forestier, L., Fayon, F., Vu Huynh, T., Allier, T., Nour, Z., and Massiot, D. (2012) New insights into the molecular structures, compositions, and cation distributions in synthetic and natural montmorillonite. *Chemistry of Materials*, **24**, 4376−4389.

Castellini, E., Berthold C., Malferrari D., and Bernini, F. (2013) Sodium hexametaphosphate interaction with 2:1 clay minerals illite and montmorillonite. *Applied Clay Science*, **83−84**, 162−170.

Che, C., Glotch, T.D., Bish, D.L., Michalski, J.R., and Xu, W. (2011) Spectroscopic study of the dehydration and/or dihydroxylation of phyllosilicate and zeolite minerals. *Journal of Geophysical Research*, **116**, E05007.

Chen Y., Shaked, D., and Banin, A. (1979) The role of structural iron III in the UV absorption by smectites. *Clay Minerals*, **14**, 93−201.

Chipera, S.J. and Bish, D.L. (2001) Baseline studies of The Clay Minerals Society Source Clays: Powder X-ray diffraction analyses. *Clays and Clay Minerals*, **49**, 398−409.

Costanzo, P.M. and Guggenheim, S. Guest Editors (2001) Baseline Studies of the Clay Minerals Society Source Clays. *Clays and Clay Minerals*, **49**, 371−452.

De Jong, B.H.W.S., Van Hoek, J., Veeman, W.S., and Manson, D.V. (1987) X-ray diffraction and ^{29}Si magic-angle-spinning NMR of opals: Incoherent long- and short-range order in opal-CT. *American Mineralogist*, **72**, 1195−1203.

Finck, N., Schlegel, M.L., and Bauer, A. (2015) Structural iron in dioctahedral and trioctahedral smectites: A polarized XAS study. *Physics and Chemistry of Minerals*, **42**, 847−859.

Finnie, K.S., Thompson, J.G., and Withers, R.L. (1994) Phase transitions in cristobalite and related structures studied by variable temperature infra-red emission spectroscopy. *Journal of Physical Chemistry of Solids*, **55**, 23−29.

Franzini, M., Leoni, L., and Saitta, M. (1975) Revisione di una metodologia analitica per fluorescenza-X, basata sulla correzione completa degli effetti di matrice. *Rendiconti della Società Italiana di Mineralogia e Petrografia*, **31**, 365−378.

Gattullo, C.E., Allegretta, I., Medici, L., Fijan, R., Pii, Y., Cesco, S., Mimmo, T., and Terzano, R. (2016) Silicon dynamics in the rhizosphere: Connections with iron mobilization. *Journal of Plant Nutrition and Soil Science*, **179**, 409−417.

Goldman, M., Grandinetti, P.J., Llor, A., Olejniczak, Z., Sachleben, J.R., and Zwanziger, J.W. (1992) Theoretical aspects of higher-order truncations in solid-state NMR. *Journal of Chemical Physics*, **97**, 8947−8960.

Gualtieri, A. F. (2000) Accuracy of XRPD QPA using the combined Rietveld-RIR method. *Journal of Applied Crystallography*, **33**, 267−278.

Guggenheim, S. and Koster van Groos, A.F. (1992) High-pressure differential thermal analysis (HP-DTA) I. Dehydration reactions at elevated pressures in phyllo-

silicates. *Journal of Thermal Analysis*, **38**, 1701−1728.

Guggenheim, S. and Koster van Groos, A.F. (2001) Baseline studies of The Clay Minerals Society Source Clays: Thermal analysis. *Clays and Clay Minerals*, **49**, 430−440.

Hahn, J.E., Scott, R.A., Hodgson, K.O., Doniach, S., Desjardins, S.R., and Solomon, E.I. (1982) Observation of an electric quadrupole transition in the X-ray absorption spectrum of a Cu(II) complex. *Chemical Physics Letter*, **88**, 595−598.

Harris, R.K., Becker, E.D., Cabral de Menezes, S.M., Goodfellow, R., and Granger, P. (2001) NMR nomenclature. Nuclear spin properties and conventions for chemical shifts. *Pure and Applied Chemistry*, **73**, 1795−1818.

Karickhoff, S.W. and Bailey, G.W. (1973) Optical absorption spectra of clay minerals. *Clays and Clay Minerals*, **21**, 59−70.

Kihara, K. (1981) Addenda and corrigendum for "On the split-atom model for hexagonal tridymite." *Zeitschrift für Kristallographie*, **157**, 93.

Kogel, J.E. and Lewis, S.A. (2001) Baseline studies of The Clay Minerals Society Source Clays: Chemical analysis by inductively coupled plasma-mass spectroscopy (ICP-MS). *Clays and Clay Minerals*, **49**, 387−392.

Larson, A.C. and Von Dreele, R. (1994) *General Structure Analysis System (GSAS)*. Los Alamos National Laboratory Report LAUR, 86−748.

Leoni, L. and Saitta, M. (1976) X-ray fluorescence analysis of 29 trace elements in rock and mineral standards. *Rendiconti della Società Italiana di Mineralogia e Petrografia*, **32**, 497−519.

Lu, L., Cai, J., and Frost, R.L. (2010) Near infrared spectroscopy of stearic acid adsorbed on montmorillonite. *Spectrochimica Acta Part A*, **75**, 960−963.

Madejová, J. (2003) FTIR techniques in clay mineral studies. *Vibrational Spectroscopy*, **31**, 1−10.

Madejova, J. and Komadel, P. (2001) Baseline studies of The Clay Minerals Society Source Clays: Infrared methods. *Clays and Clay Minerals*, **49**, 410−432.

Madejová, J., Bujdák, J., Janek, M., and Komadel, P. (1998) Comparative FT-IR study of structural modifications during acid treatment of dioctahedral smectites and hectorite. *Spectrochimica. Acta A*, **54**, 1397−1406.

Malferrari, D., Brigatti, M.F., Laurora, A., Medici, L., and Pini, S. (2006) Thermal behavior of Cu(II)-, Cd(II)-, and Hg(II)-exchanged montmorillonite complexed with cysteine. *Journal of Thermal Analysis and Calorimetry*, **86**, 365−370.

Malferrari, D., Brigatti, M.F., Laurora, A., Pini, S., and Medici, L. (2007) Sorption kinetics and chemical forms of Cd(II) sorbed by thiol-functionalized 2:1 clay minerals. *Journal of Hazardous Materials*, **143**, 73−81.

Malferrari, D., Brigatti, M.F., Marcelli, A., Chu, W., and Wu Z. (2008) Modification of Hg complexes in layered silicates with temperature: An *in situ* XAS study. *Microporous and Mesoporous Materials*, **107**, 128−133.

Manceau, A., Drits, V., Lanson, B., Chateigner, D., Wu, J., Huo D., Gates W.P., and Stucki J. (2000) Oxidation–reduction mechanism of iron in dioctahedral smectites, II. Crystal chemistry of reduced Garfield nontronite. *American Mineralogist*, **85**, 153−172.

Mercier, L. and Detellier, C. (1994) Intercalation of tetraalkylammonium cations into smectites and its application to internal surface-area measurements. *Clays and Clay Minerals*, **42**, 71−76.

Men, Y., Gnaser, H., and Ziegler, C. (2003) Adsorption/desorption studies on nanocrystalline alumina surfaces. *Analytical and Bioanalytical Chemistry*, **7**, 912−916.

Mermut, A.R. and Cano, A.F. (2001) Baseline studies of The Clay Minerals Society Source Clays: Chemical analyses of major elements. *Clays and Clay Minerals*, **49**, 381−386.

MNOVA 9.1.0 software (2012) Mestrelab Research S.L., Santiago de Compostela, Spain.

Moronta, A., Taylor, S., and Breen, C. (2002) Adsorption of olefins on aluminum- and aluminum/tetramethyl-ammonium-exchanged bentonites. *Clays and Clay Minerals*, **50**, 265−271.

Newville, M. (2001) IFEFFIT: Interactive XAFS analysis and FEFF fitting. *Journal of Synchrotron Radiation*, **8**, 322−324.

Ortega-Castro, J., Hernández-Haro, N., Muñoz-Santiburcio, D., Hernández-Laguna, A., and Sainz-Díaz, C.I. (2009) Crystal structure and hydroxyl group vibrational frequencies of phyllosilicates by DFT methods. *Journal of Molecular Structure: THEOCHEM*, **912**, 82−87.

Peacor, D.R. (1973) High-temperature single-crystal study of the cristobalite inversion. *Zeitschrift für Kristallographie*, **138**, 274−298.

Petit, S, Madejova, J., Decarreau, A., and Martin, F. (1999) Characterization of octahedral substitutions in kaolinites using near infrared spectroscopy. *Clays and Clay Minerals*, **47**, 103−108.

Ravel, B. and Newville, M. (2005) ATHENA, ARTEMIS, HEPHAESTUS: Data analysis for X-ray absorption spectroscopy using IFEFFIT. *Journal of Synchrotron Radiation*, **12**, 537−541.

Sherman, D.M. and Waite, T.D. (1985) Electronic spectra of Fe^{3+} oxides and oxide hydroxides in the near IR to near UV. *American Mineralogist*, **70**, 1262−1269.

Shulman, R.G., Yafet, Y., Eisenberger, P., and Blumberg, W.E. (1976) Observations and interpretation of X-ray absorption edges in iron compounds and proteins. *Proceedings of the National Academy of Sciences of the United States of America*, **73**, 1384−1388.

Smith, G. and Alexander, L.E. (1963): Refinement of the atomic parameters of α-quartz. *Acta Crystallographica*. **16**, 462−471.

Takahashi, T., Kanehashi, K., and Saito, K. (2008) First evidence of multiple octahedral Al sites in Na-montmorillonite by ^{27}Al multiple quantum MAS NMR. *Clays and Clay Minerals*, **56**, 520−525.

Takahashi, T., Ohkubo, T., Suzuki, K., and Ikeda, Y. (2007) High resolution solid-state NMR studies on dissolution and alteration of Na-montmorillonite under highly alkaline conditions. *Microporous and Mesoporous Materials*, **106**, 294−297.

Toby, B.H. (2001) EXPGUI, a graphical interface for GSAS. *Journal of Applied Crystallography*, **34**, 210−213.

van Olphen, H. and Fripiat, J.J., Editors (1979) *Data Handbook for Clay Minerals and Other Non-metallic Minerals*. Pergamon Press, Oxford, England, 346 pp.

Vantelon, D., Montarges-Pelletier, E., Michot, L.J., Briois, V., Pelletier, M., and Thomas, F. (2003) Iron distribution in the octahedral sheet of dioctahedral smectites. An Fe *K*-edge X-ray absorption spectroscopy study. *Physics and Chemistry of Minerals*, **30**, 44−53.

Vedder, W. (1964) Correlations between infrared spectrum and chemical composition of mica. *American Mineralogist*, **49**, 736−768.

Viani, A., Gualtieri, A., and Artioli, G. (2002) The nature of disorder in montmorillonite by simulation of X-ray powder patterns. *American Mineralogist*, **87**, 966−975.

Westre, T.E., Kennepohl, P., DeWitt, J.G., Hedman, B., Hodgson, K.O., and Solomon, E.I. (1997) A multiplet analysis of Fe *K*-edge 1s→3d pre-edge features of iron complexes. *Journal of American Chemical Society*, **119**, 6297−6314.

Wilke, M., Farges, F., Petit, P.-E., Brown, G.E., and Martin, F. (2001) Oxidation state and coordination of Fe in minerals:

An Fe K-XANES spectroscopic study. *American Mineralogist*, **86**, 714−730.

Woessner, D.E. (1989) Characterization of clay minerals by [27]Al nuclear magnetic resonance spectroscopy. *American Mineralogist*, **74**, 203−215.

Young, H.D. (1962) *Statistical Treatment of Experimental Data*. McGraw-Hill Book Company, New York.

Zhu, R, Chen, Q., Zhou, Q., Xi, Y., and Zhu, J. (2016) Adsorbents based on montmorillonite for contaminant removal from water: A review. *Applied Clay Science*, **123**, 239−258.